J Nanostruct 9(3): 414-428, Summer 2019

RESEARCH PAPER

An Efficient Co-Precipitation Synthesis of $BaZr_{1-x}Co_xO_3$ Nanoparticles: Structural, Optical and Magnetic Properties

D. EL-Said Bakeer, Abdel-Hamed Sakr, H. A. Motaweh, W. El-Sokary*

Physics Department, Faculty of Science, Damanhour University, Damanhour, Egypt

ARTICLE INFO

Article History:
Received 05 April 2019
Accepted 13 June 2019
Published 01 July 2019

Keywords:
$BaZrO_3$ Nanoparticles
Co-Precipitation Method
FTIR
Magnetic Properties
Single Oscillator Model

ABSTRACT

In this study, $BaZr_{1-x}Co_xO_3$ nanoparticles, x = 0.00, 0.04, 0.06, 0.08, 0.10 and 0.20, are synthesized through co-precipitation method. Therefore, structural, optical and magnetic properties have been investigated. The cubic perovskite structure is confirmed by X-ray diffraction (XRD) and Fourier transform infrared (FTIR) spectroscopic measurements. The average crystallite size and micro strain are calculated by Williamson-hall analysis and they have been found to increase by increasing Co^{2+} content. More emphasis is given for the calculation of the optical parameters from UV–visible absorption spectra. The optical bandgap is found to be decreasing; on the other hand Urbach energy increases with the increase in Co^{2+} content. The refractive index of the samples obeys the single-oscillator model and the dispersion parameters such as single oscillator energy, dispersion energy, and lattice dielectric constant are calculated and their variations with Co^{2+} content are reported. The undoped $BaZrO_3$ nanoparticles exhibit unexpected superparamagnetic behavior and ferromagnetic hysteresis at room temperature for $BaZr_{1-x}Co_xO_3$, x=0.10 and 0.20. With increasing in Co^{2+} content, the concentration of oxygen vacancies increases and as a result the magnetic properties are improved. Thus, the most significant result of the present work is the modification of optical constants and the improvement of magnetic properties of $BaZrO_3$ nanoparticles by partial Co^{2+} substitution.

How to cite this article
EL-Said Bakeer D, Sakr AH, Motaweh HA, El-Sokary W. An Efficient Co-Precipitation Synthesis of $BaZr_{1-x}Co_xO_3$ Nanoparticles: Structural, Optical and Magnetic Properties. J Nanostruct, 2019; 9(3): 414-428. DOI: 10.22052/JNS.2019.03.003

INTRODUCTION

In recent years, ceramic materials with perovskite structure ABO_3 (A =Ba, Sr, Ca, Mg, Pb; B = Zr, Ti, Sn) have attracted considerable attention due to its interesting electronic properties [1]. These materials have various phase transitions (ferroelectric, ferroelastic, magnetic, and superconducting) and have been used as insulators [2], capacitors [3] and superconductors [4]. Barium zirconate ($BaZrO_3$),as one of the alkaline earth metals with a cubic structure, has a great interesting properties due to its high proton conductivity coupled with good chemical and mechanical stability [5]. Accordingly, it can be used for a range of electrochemical applications, such as fuel cells, separation membranes and steam electrolysis [6]. $BaZrO_3$ is a material that has a very high melting temperature (about 2,600 °C), a very high stability under heating, low thermal coefficient and poor thermal conductivity expansion which make it a suitable material for crucibles, usable in melting processes of high critical temperature superconductors [7,8] and substrates for thin films deposition. In addition, it is useful for the production of hydrogen sensor applications [9]. As a matter of fact, the fine $BaZrO_3$ powder is good for the fabrication of multi-layer ceramic capacitor [10]. Moreover, it has promising

* *Corresponding Author Email: d_bakeer2010@yahoo.com*

applications in tunable filters, generators, phase shifters, and phased array antennas since its solid solutions with $BaTiO_3$ have a very high electric field tuning of the dielectric constant [11,12]. Moreover, it is a noteworthy that alkaline-earth zirconate is a potential material for humidity sensor [13]. Nowadays there are numerous world-wide studies on the ferromagnetism induction to this nonmagnetic perovskite material by doping transition metals, intended to be applied in the emerging field of spintronics, data- storage media, and multiple-state memories [14,15]. $BaZrO_3$ has been synthesized in various methods such as solvothermal [16], co-precipitation [17], sol-gel [18], conventional solid-state reaction [19], laser ablation [20], ballmilling [21], aerosol [22], and microemulsion [23,24]. Among these approaches, the co-precipitation method is a convenient way to synthesize nanosized particles from aqueous anion/cation salt solutions due to its simplicity, good mixing of starting materials, relatively easy control of chemical composition, effective route for better control of the particle sizes and shapes, controlling the rate of precipitation, low cost and preparation of all types of nanoparticles.

The main motivation of the present work is to synthesis a series of $BaZr_{1-x}Co_xO_3$ nanoparticles with the various compositions, x = 0.0, 0.04, 0.06, 0.08, 0.10 and 0.20 by an efficient chemical co-precipitation method and to study the desired magnetic and optical properties for their use in photo sensing and spintronic device applications. It should be noted that the detailed study of the structural, optical and magnetic properties of Co^{2+} doped $BaZrO_3$ nanoparticles has not been studied yet.

MATERIALS AND METHODS

$BaZr_{1-x}Co_xO_3$ nanoparticles, x=0.00, 0.04, 0.06, 0.08, 0.10 and 0.20 are synthesized using chemical co-precipitation method. Stoichiometric amounts of analytical grade chemical reagents, cobalt chloride ($CoCl_2.6H_2O$), barium chloride ($BaCl_2.6H_2O$) zirconium chloride ($ZrOCl_2.8H_2O$), are dissolved in distilled water to get homogeneous aqueous solutions. $BaCl_2.6H_2O$ solution is mixed properly using magnetic stirrer and heating till the temperature reaches 75°C.Then the buffer solution (NaOH) is added to the salt solution till the pH is adjusted to 12.0. Then $ZrOCl_2.8H_2O$ is added slowly producing white precipitates. The PVA (polyvinyl acetal) is being added to avoid agglomeration of particles and to protect particles from atmospheric. Simultaneous heating and with continuous stirring of solution till the temperature reaches 95°C and keep it constant for 1 h. The synthetic reaction occurs as follows [25]:

$$Bacl_2.2H_2O + ZrOCl_2.8H_2O + 4NaOH \xrightarrow{95°C} BaZrO_3 + 4NaCl + 12H_2O \quad (1)$$

The precipitate is washed using de-ionized water to remove unwanted salt residues and is then dried at 100 ºC for 24 h to remove remaining water. Next, the dried powder is calcined at 1100°C for 2 h to improve the crystalline properties.

Structural and phase purity studies of $BaZr_{1-x}Co_xO_3$ nanoparticles are investigated by X-ray powder diffraction using Bruker D8 advance powder diffractometer with Cu-Kα radiation (λ = 1.54056 Å) in the 2θ range 10° - 80°. The size and shape of the synthesized nanoparticles are checked using Jeol transmission electron microscope JEM- 2100, operated at 200 kV. The elemental composition and doping effect of Co^{2+} in $BaZrO_3$ host lattice is investigated using energy dispersive X-ray spectroscopy (EDS) on JSM-IT100LA SEM. Fourier transform infrared (FTIR) spectrum is recorded on FTIR 8400S Shimadzu spectrophotometer in KBr pellets. Ultraviolet–visible (UV–vis) absorption spectra of $BaZr_{1-x}Co_xO_3$ nanoparticles are recorded using Evolution 300 spectrophotometer. A vibrating sample magnetometer (VSM), Lakeshore 7410, is applied to investigate the magnetic properties of $BaZr_{1-x}Co_xO_3$ nanoparticles, $0.00 \leq x \leq 0.20$ at room temperature.

RESULTS AND DISCUSSIONS

The XRD patterns of $BaZr_{1-x}Co_xO_3$ nano powders heat treated at 1100°C for 2 h are shown in Fig. 1. The $BaZrO_3$ phase is confirmed by comparison with the XRD patterns for (JCPDS) card No. 006-0399 [24,25]. All diffraction peaks of nanoparticles are indexed as a cubic perovskite structure. No other impurity phases are detected by XRD patterns. The diffraction patterns confirm that all the prepared samples are monophasic in nature. Actually, the sharpness of the peaks indicates the higher degree of crystallinity of the nanoparticles. A monotonic shift in diffraction pattern towards the higher angle is observed, which clearly indicates the formation of the solid solution $BaZr_{1-x}Co_xO_3$. The

unit cell parameter "*a*" calculated from the XRD data is *a* = 4.184Å, which is in good agreement with the data reported in JCPDS file (JCPDS 006-0399) [25].The unit cell parameter is found to be decreased as the Co^{+2} content increases (see the inset of Fig. 1) obeying Vegard's law [26] and their values are listed in Table 1. The lattice contraction of host lattice is associated to the smaller ionic radius of Co^{+2} (0.79 Å) as compared with Zr^{+4} (0.86 Å), which may lead to the substantial solubility of Co^{+2} ions in $BaZrO_3$ host lattice. In fact, this result can be confirmed by the observed shift of the (110) peak towards the higher diffraction angle as the concentration of Co^{2+} increases (see Fig. 2).

The Goldschmidt tolerance factor which has been used extensively to predict the stability of the perovskite structure can be defined as [27]:

$$t_f = \frac{r_{Ba^{2+}} + r_{O^{2-}}}{\sqrt{2}\left((1-x)\,r_{Zr^{4+}} + x r_{Co^{2+}} + r_{O^{2-}}\right)} \qquad (2)$$

as given in Table 1. This indicates that there is no structural change in the compositions with incorporation of Co^{2+} content. The increase in tolerance factors is simply attributed to the structural disorder in the composition.

The effect of Co^{2+} substitution for the Zr^{4+} can be expressed using Kröger-Vink notation as:

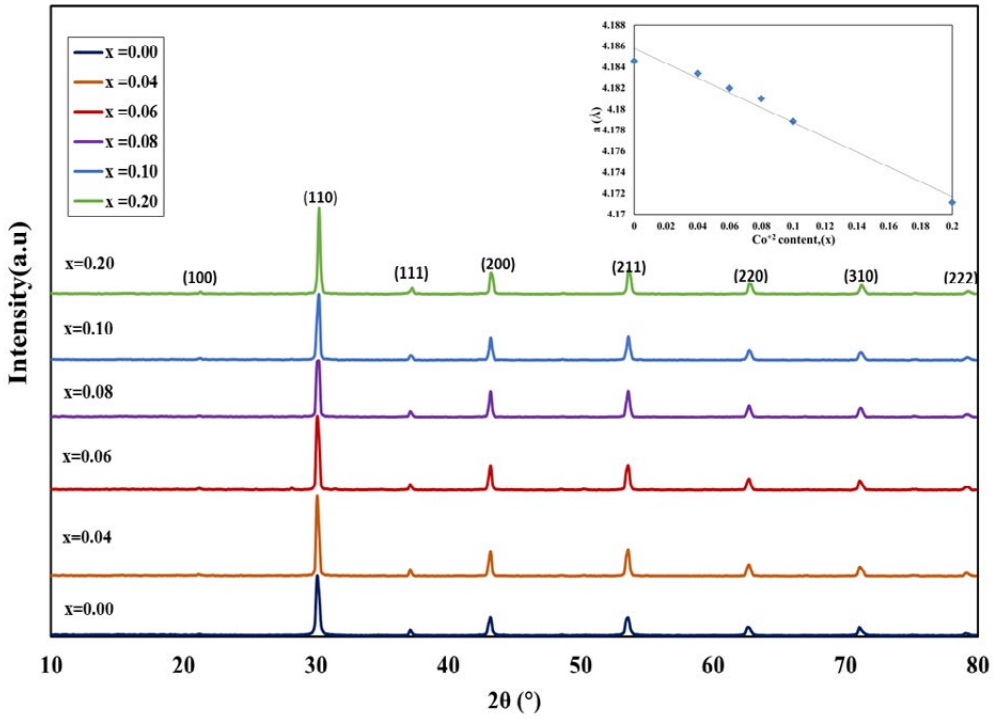

Fig. 1. XRD patterns of $BaZr_{1-x}Co_xO_3$ nanoparticles, $0.00 \le x \le 0.20$.The inset shows the variation of unit cell parameter (*a*) with Co^{2+} content, x for $BaZr_{1-x}Co_xO_3$ nanoparticles.

Table 1. Unit cell parameter (*a*), tolerance factor (t_f), crystallite size (D_{XRD}) and micro strain (ε) of $BaZr_{1-x}Co_xO_3$ nanoparticles ($0.00 \le x \le 0.20$)

Co^{2+}content (x)	unit cell parameter (*a*) (A°)	t_f	D_{XRD} (nm)	$\varepsilon \times 10^{3-}$
0.00	4.185	1.091	46.218	1.14
0.04	4.183	1.100	49.519	1.28
0.06	4.182	1.105	51.353	1.12
0.08	4.181	1.109	53.328	1.18
0.10	4.179	1.115	59.001	1.32
0.20	4.171	1.139	66.982	1.35

$$ZrO_2 + CoO \rightarrow Zr_{Zr} + Co_{Zr} + V_{\ddot{Zr}} + 3O_O \quad (3)$$

Where, Zr_{Zr} indicates a zirconium ion sitting on an zirconium lattice site, with neutral charge, Co_{Zr} indicates a cobalt ion sitting on an zirconium lattice site, with neutral charge and V_{Zr} indicates a zirconium vacancy, with double positive charge.

According to this substitution every Co^{2+} ions insert into the B-site, one vacancy with double positive charge must be created to maintain the charge neutrality of the perovskite structure.

The average crystallite sizes (D_{XRD}) and lattice strain ε of all the prepared samples are calculated from the full width at half max (FWHM) of the peaks using Williamson-Hall (W-H) plots [28],

$$\beta \cos\theta = \frac{k\lambda}{D_{XRD}} + 4\varepsilon \sin\theta \quad (4)$$

By plotting *β cos ϑ* against *4 sin ϑ* as shown in Fig. 3, the slope of the fitted linear directly gives the lattice strain and the average crystallite size

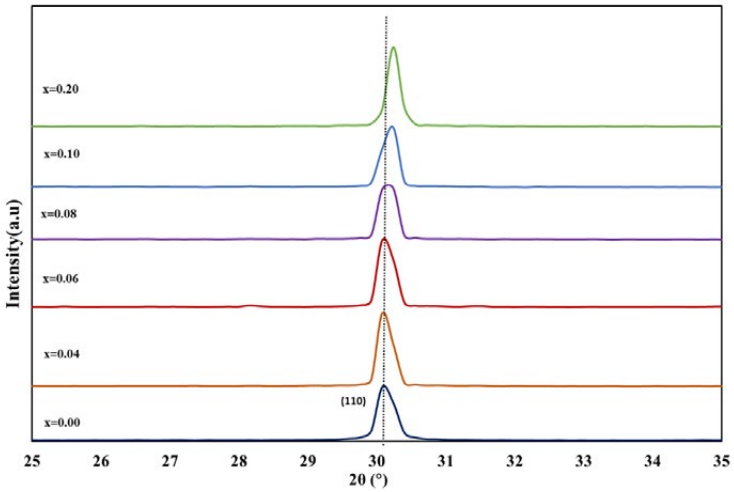

Fig. 2. Enlarged view of the XRD patterns around the major peak (110).

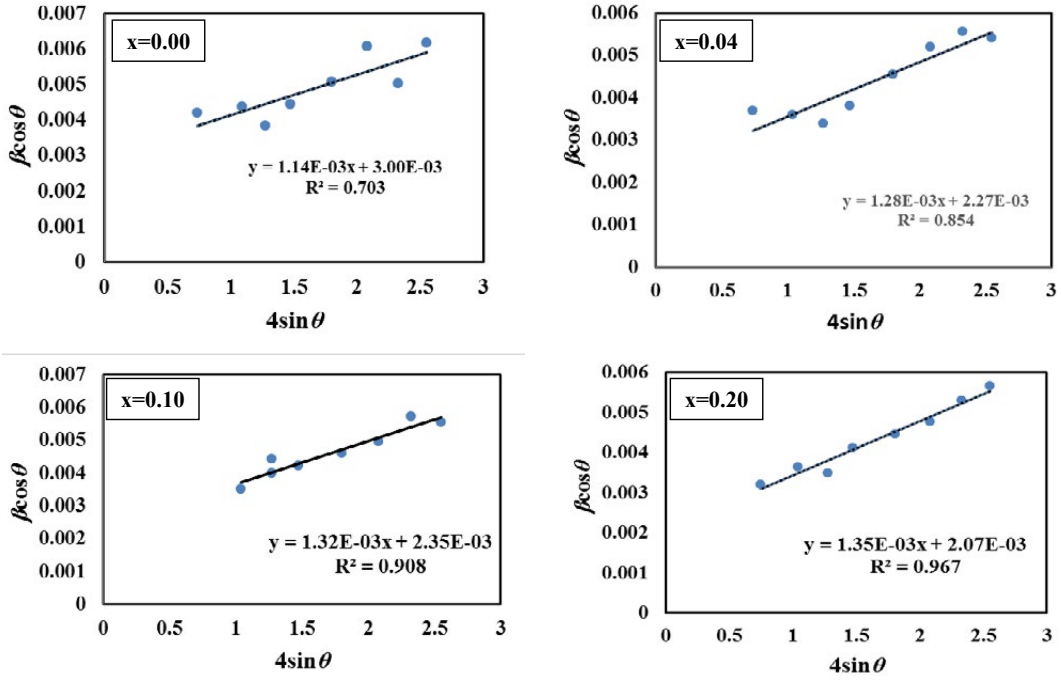

Fig. 3. Plots of βCosθ Vs. 4sinθ of $BaZr_{1-x}Co_xO_3$ nanoparticles, (a) x = 0.00, (b) x = 0.04 (c) x = 0.10 and (d) x = 0.20.

(D_{XRD}) is obtained using the intercept of the line as;

$$D_{XRD} = \frac{\lambda}{\text{intercept}} \quad (5)$$

The average crystallite size, and lattice strain obtained for all the samples are listed in Table 1. The average crystallite size is found to be in the range of 46.218–66.982 nm (Table 1). The calculated crystallite size of undoped $BaZrO_3$ is higher than that reported by single-step combustion method (30 nm)[29] and sol–gel auto combustion method (24 nm) [30]. The other important observation is the crystallite size of Co^{2+} doped samples are greater than those of the undoped sample. The lattice strain of all compositions is found to increase with an increase in Co^{2+} content. This compressive strain may be due to lattice shrinkage.

TEM study is carried out to investigate the shape, size of the prepared nanoparticles. Figs. 4 (a-d) show the TEM micrographs of $BaZr_{1-x}Co_xO_3$, x = 0.00, 0.06, 0.08 and 0.2. We can observe from the micrographs the formation of spherical particles and pseudo- particles in nano scale with nominal agglomeration due to heating the powder at 1100 ºC in air. In addition, it is observed that the particles show little distortion without any secondary phases. As a matter of fact, these results are consistent with those obtained from XRD. The average particle size is found in the range of 40-65 nm. Furthermore, some bigger particles are seen in the micrographs, which may be due to the aggregation of smaller particles. It is worth noting that the spherical particles slightly disappear and the pseudo- particles appear as the Co^{2+} content increases. The different particle shapes result simply from the difference in crystal faces supporting on the carbon grids used for TEM measurement as well as the concentration of the solvent. Therefore, we can say that the size and shape of $BaZrO_3$ microcrystals can be controlled by

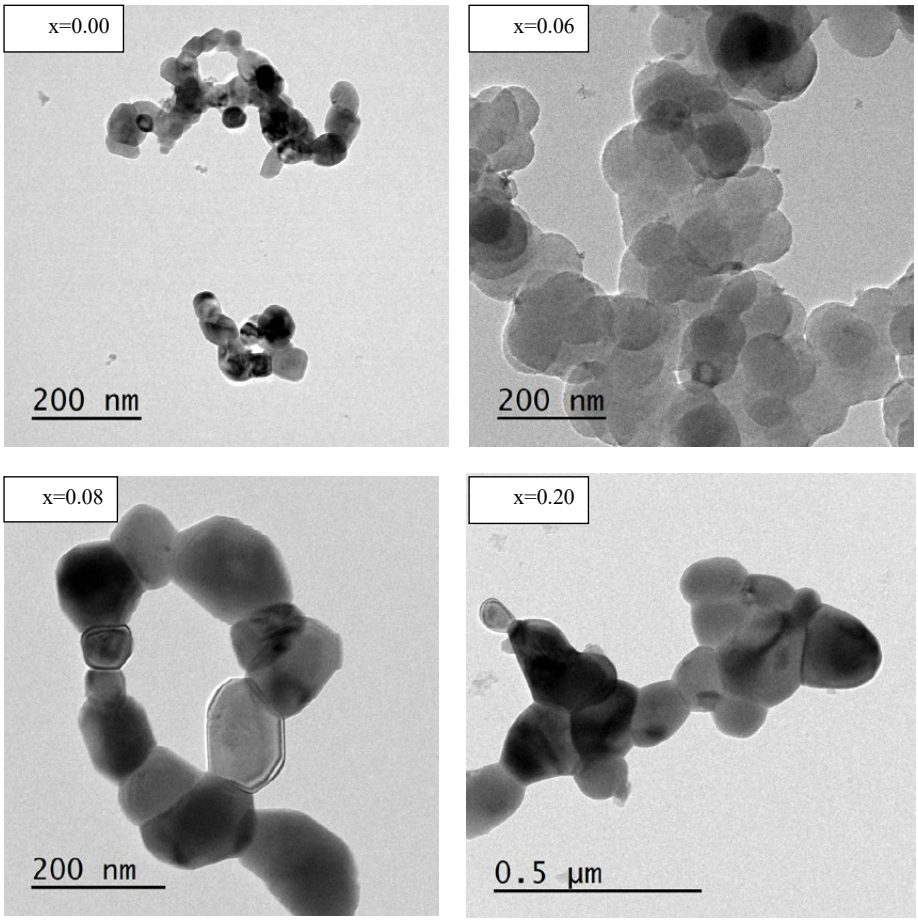

Fig. 4. TEM micrographs of $BaZr_{1-x}Co_xO_3$, (a) x = 0.00, (b) x = 0.06 (c) x = 0.08 and (d) x = 0.20.

the experimental conditions.

Typical EDS patterns of $BaZr_{1-x}Co_xO_3$ nanoparticles with x = 0.00 and 0.10 are shown in Fig. 5. The presence of Ba, Co, Zr, and O peaks affirms the formation of $BaZr_{1-x}Co_xO_3$ solid solution and confirms the incorporation of Co^{2+} in the $BaZrO_3$ host lattice. The chemical compositions of all elements are found to be in close agreement to the experimentally calculated composition.

The FT-IR spectra for $BaZr_{1-x}Co_xO_3$, $0.00 \leq x \leq 0.20$ are illustrated in Fig. 6. There is no evidence for the presence of any organic intermediates in the sample. This corroborates the XRD results. The strong vibrational mode at 531 cm^{-1} can be attributed to the stretching vibrations of Zr–O–Zr octahedral, which agrees well with the literature [25,29]. The characteristic peak around 1455 corresponds to the bending vibrations of the absorbed water molecules and stretching vibrations of hydroxyl (–OH) group. When Co^{2+} is doped at the Zr site of $BaZrO_3$, a particular trend of shifting of peaks is observed toward higher energy. Hence, this suggests the formation of more stable compounds with an increase in the Co^{2+} content. This might be due to the combined effect of the ionic radius of Co^{2+} being lower than that of Zr^{4+} and the B-site vacancies created (as discussed in previous section), which produces little stress on ZrO_6 perovskite octahedra. As a result, cell volume decreases with the increase in the Co^{2+} content, and hence this enhances the bond strength resulting in a more stable compound. Subsequently, this causes the shifting of wave number toward the right, suggesting the

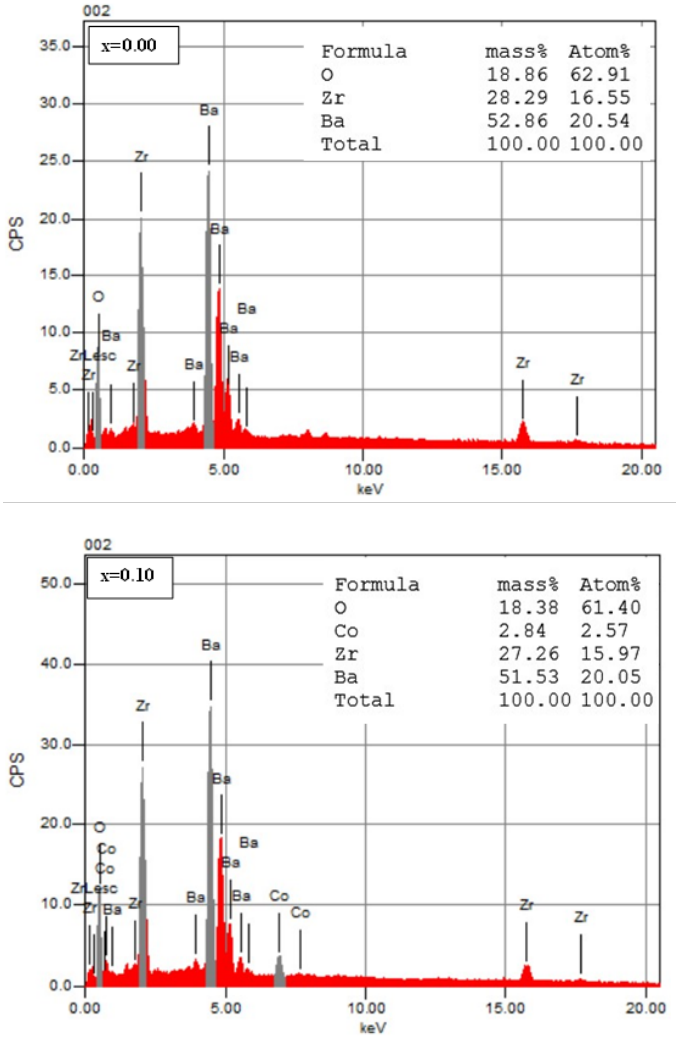

Fig. 5. EDS spectrum of $BaZr_{1-x}Co_xO_3$, (a) x = 0.00, (b) x = 0.10.

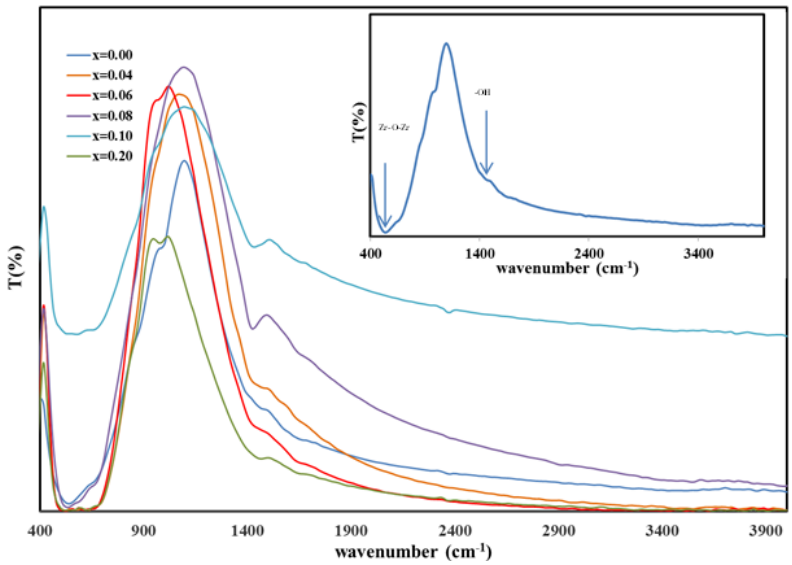

Fig. 6. FT-IR spectra of $BaZr_{1-x}Co_xO_3$ nanoparticles, $0.00 \leq x \leq 0.20$.

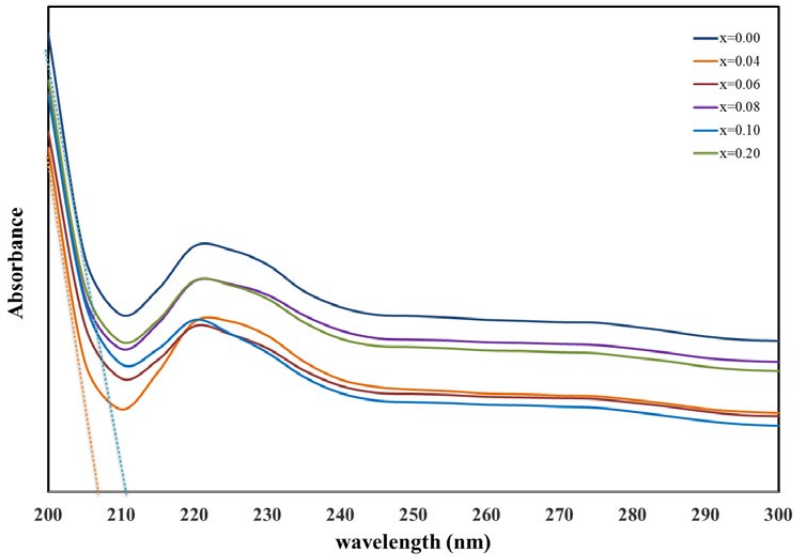

Fig. 7. UV absorption spectra of $BaZr_{1-x}Co_xO_3$ nanoparticles.

formation of more stable compounds.

The energy band structure of pure and Co^{2+} doped $BaZrO_3$ nanoparticles is investigated using the UV-vis spectroscopy. The absorption spectra of $BaZr_{1-x}Co_xO_3$ nanoparticles are shown in Fig. 7. Strong absorption band around 220 nm is mainly due to the optical transitions from valence band to conduction band. Moreover, an absorption tail towards IR region is observed. In fact, the absorption band edge wavelength shifts to a lower wave length (blue shift), indicating that the absorption behavior might be affected by the crystallite and the particle size [31].

The absorption coefficient, α, is calculated from the measured values of *R* and *T* using the following equation [32]

$$\alpha = \left(\frac{(1-R)^2}{2R} \right) \quad (6)$$

The optical band gap (E_{opt}) can be calculated

from the Tauc relation [33]:

$$\alpha h\upsilon = B\,(h\upsilon - E_{opt})^n \quad (7)$$

where n is an index determined by the nature of the electron transition during the absorption process, (n = 1/2 for allowed direct transition E^d_{opt}, and n=2 for allowed indirect transition E^i_{opt}) and *B* is a constant depending on the transmittance properties of E_{opt}. The present results are found to obey Eq. (7). The quantity $(\alpha h\upsilon)^2$ is plotted against photon energy ($h\upsilon$) for different concentration of Co^{2+} ions ,as shown in Figs. 8(a-e). The indirect band-gap energies for $BaZr_{1-x}Co_xO_3$ nanoparticles are given by the intersection of the straight line with the horizontal axis. The indirect optical band gap energies are listed in Table 2. It is observed that the indirect optical band gap energy for

Table 2. Influence of Co^{2+} content on the optical parameters, calculated from UV-vis spectra, of $BaZr_{1-x}Co_xO_3$ nanoparticles ($0.00 \le x \le 0.20$)

Co^{2+} content (x)	E^i_{opt} (eV)	E_u (eV)	$E_d \times 10^{-3}$ (eV)	E_O (eV)	E_g (eV)	$S_O \times 10^{-8}$ $(nm)^{-2}$	λ_O (nm)	ε_l
0.00	4.00	0.608	5.01	5.14	2.57	1.67	241.90	2.35
0.04	3.90	0.790	0.91	4.96	2.48	0.33	234.50	2.69
0.06	3.85	0.877	3.04	4.94	2.47	1.00	248.11	3.59
0.08	3.82	1.259	2.56	4.76	2.38	1.00	231.96	4.42
0.10	3.80	1.307	3.61	4.16	2.08	1.00	294.42	4.12
0.20	3.78	1.538	0.477	3.70	1.85	0.11	340.70	4.50

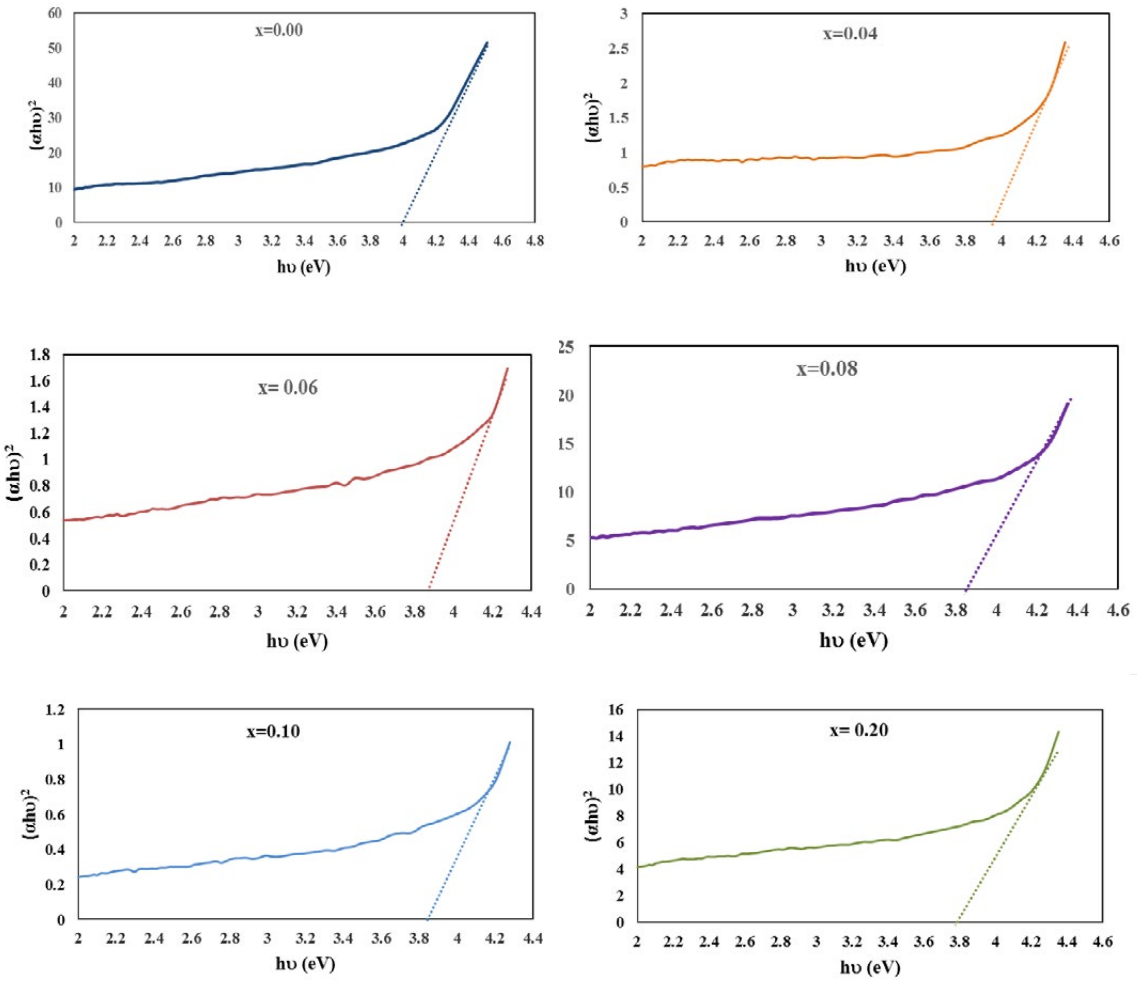

Fig. 8. Tauc plots of $BaZr_{1-x}Co_xO_3$ nanoparticles, $0.00 \le x \le 0.20$.

$BaZrO_3$ is 4.00 eV which is lower than the previous reported value [34] and its value shows a decrease as the Co^{2+} content increases. The smaller value of optical band gap of undoped $BaZrO_3$ in comparison to the reported value may be due to local states formation near the band edge [35]. As a matter of fact, the decrease in optical energy band gap could be due to the increase of the particle size and the increase of density of localized state in the conduction band [36]. This can be explained on the basis of Bras effective mass model [37] according to which the measured band gap, E_g can be expressed as a function of particle size as follows:

$$E_g = E_g^{bulk} \frac{h^2}{8m_0 D^2}\left(\frac{1}{m_e}+\frac{1}{m_h}\right) - \frac{1.8e^2}{4\pi\varepsilon\varepsilon_0} \quad (8)$$

where D is the particle size, E_g^{bulk} is the bulk energy gap, m_e is the effective mass of the electron, m_h is the effective mass of the holes. ε and ε_0 are the relative permittivity and free space permittivity, respectively.

The absorption coefficient near the fundamental absorption edge is exponentially dependent on the incident photon energy and obeys the empirical Urbach relation,

where ln α varies as a function of hυ. The Urbach energy E_u , the width of band tails of localized states into the gap, can be calculated by the following relation [38],

$$\alpha = \alpha_0 \exp\left(\frac{h\upsilon}{\Delta E_u}\right) \quad (9)$$

where α_0 is constant, This equation can be written as:

$$\ln\alpha = \ln\alpha_0 + \frac{h\upsilon}{\Delta E_u} \quad (10)$$

The variation of (ln α) with the photon energy was presented in Fig. 9a. A clear dependence of

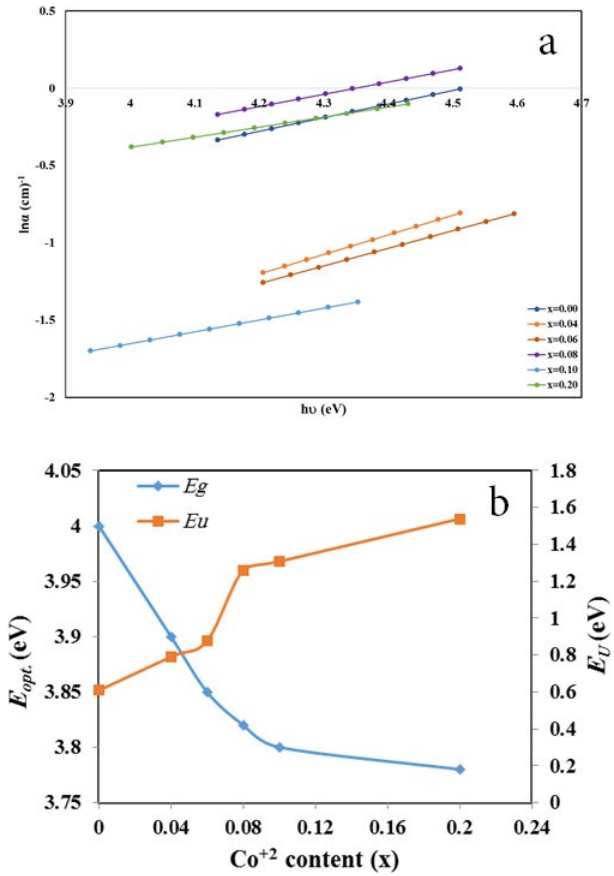

Fig. 9. a) Urbach plots of $BaZr_{1-x}Co_xO_3$ nanoparticles. b) The variation of optical band gap and Urbach energy with Co^{2+} content (x).

(ln α) on the doping and the photon energy is observed in each sample. The experimental value for the Urbach energy, E_u, of the localized state was obtained from the slope of the linear portion of curves (slope=1/ E_u) and were tabled in Table 2. It is observed that the value of Urbach energy E_u increases with the increase in the grain size.

What's more, it is noted that there is an inverse relationship between the optical band gap E_{opt}^{i} and the width of the localized states E_u, as shown in Fig. 9b. It can be observed that as the optical band gap decreases, the magnitude of defect energy (Urbach energy) increases. The decrease in optical band gap may be due to the formation of sub-band states between the valence and conduction bands resulting in the narrowing of the band gap. Conversely, the effective increase in Urbach energy with an increase of Co^{2+}content indicates that the number of defect levels below the conduction band increases to the extent that the band edge is shifted deep into the forbidden gap. A similar behaviour is observed in Nd-doped $BaZrO_3$ nanoparticles [27].

For semiconductors materials (where $K^2 >> n^2$), there exists a relationship

between R and n given by [39]:

$$R = \frac{n^2 - 1}{n^2 + 1} \tag{11}$$

The refractive index of the investigated samples can be fitted by Wemple–DiDomenico relation [39]. In this model, the refractive index dispersion is studied in the region below the band gap, using the single-oscillator.

$$\left(n^2 - 1\right)^{-1} = \frac{E_o}{E_d} - \frac{1}{E_o E_d}\left(h\upsilon\right)^2 \tag{12}$$

Where hυ is the photon energy, E_o is the oscillator energy that gives quantitative information on the overall band structure of the material and E_d is the dispersion energy which is a measure of the strength of inter-band optical transition inside the material. Actually, these parameters can easily be obtained by plotting graphics of $(n^2\text{-}1)^{-1}$ versus $(h\upsilon)^2$. Fig. 10 shows $(n^2\text{-}1)^{-1}$ versus $(h\upsilon)^2$ plots of $BaZr_{1-x}Co_xO_3$ nanoparticles. The oscillator energy, E_o, and the dispersion energy, E_d, are directly determined from the slope 1/ E_o E_d of the linear portion of the curve and its intercept with ordinate axis E_o/ E_d and they are listed in Table 2. It was found that there exists a relationship between E_o and optical energy gap E_g, which can be expressed as Eo ≃ $2E_g$ [41]. Thus, the obtained results showed a decrease in E_d , E_o and E_g as the Co^{2+} content increases. These results are consistent with those obtained from Tauc relation.

The dependence of refractive index on wavelength is expressed by the following relation [42].

$$n^2 - 1 = \frac{S_O \lambda_O}{1 - \left(\frac{\lambda_O}{\lambda}\right)^2} \tag{13}$$

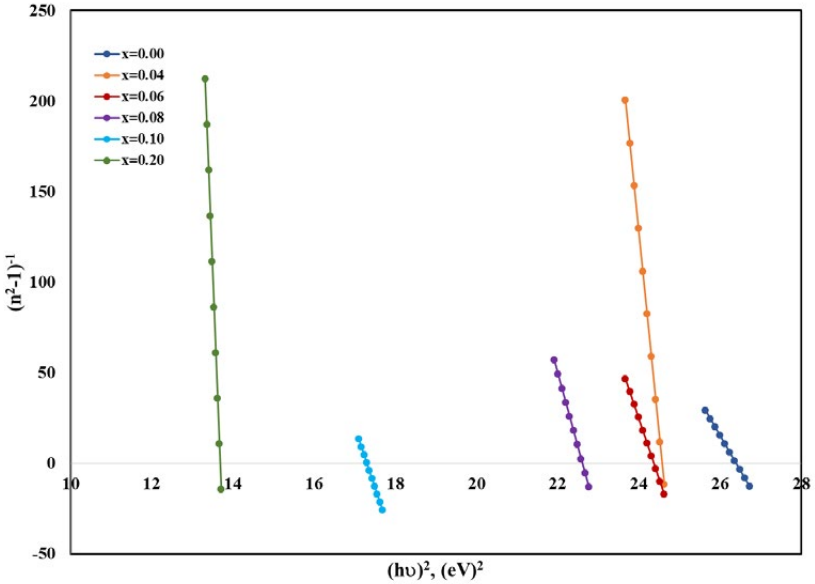

Fig. 10. Plots of $(n^2\text{- }1)^{-1}$ as a function of $(h\upsilon)^2$ for $BaZr_{1-x}Co_xO_3$ nanoparticles.

Where S_o the average oscillator strength, λ_o is an average oscillator wavelength and λ is the wavelength of incident light. The parameters λ_o and S_o values are obtained from the slope and intercept of $(n^2-1)^{-1}$ versus λ^{-2} curves (see Fig. 11) which are listed in Table 2. It is noted that the obtained parameters change with Co^{2+} content.

For further analysis of the optical data, the lattice dielectric constant is discussed according to the following relation [43]:

$$n^2 = \varepsilon_l - C\lambda^2 \quad (14)$$

Where C is constant, the value of lattice dielectric constant ε_l can be calculated from graphical representation of n^2 as a function λ^2 by extrapolating the linear part towards the shorter wavelength (Fig. 12). The intercept with the vertical axis (at $\lambda^2 = 0.0$) gives the ε_l values which are listed in Table 2. Accordingly, it is observed that the lattice dielectric constant tend to increase

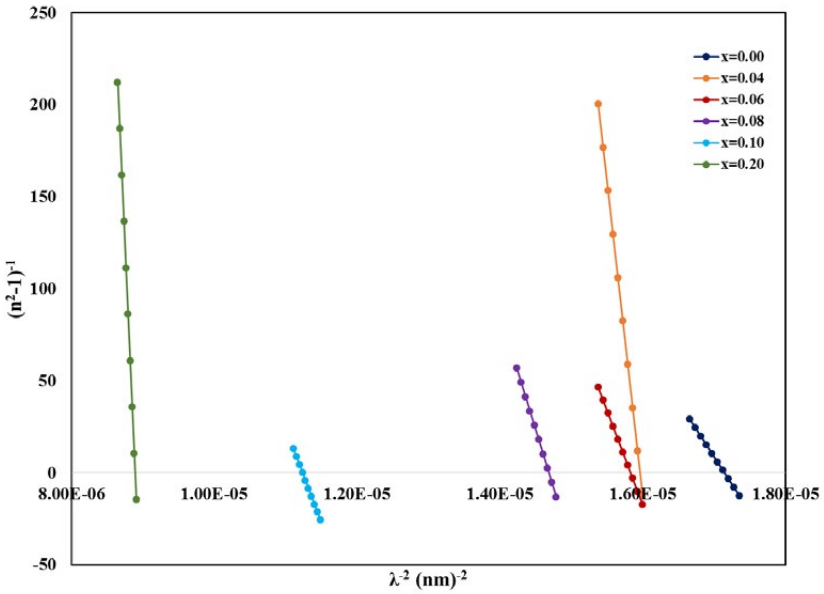

Fig. 11. Plots of $(n^2- 1)^{-1}$ as a function of l^{-2} for $BaZr_{1-x}Co_xO_3$ nanoparticles.

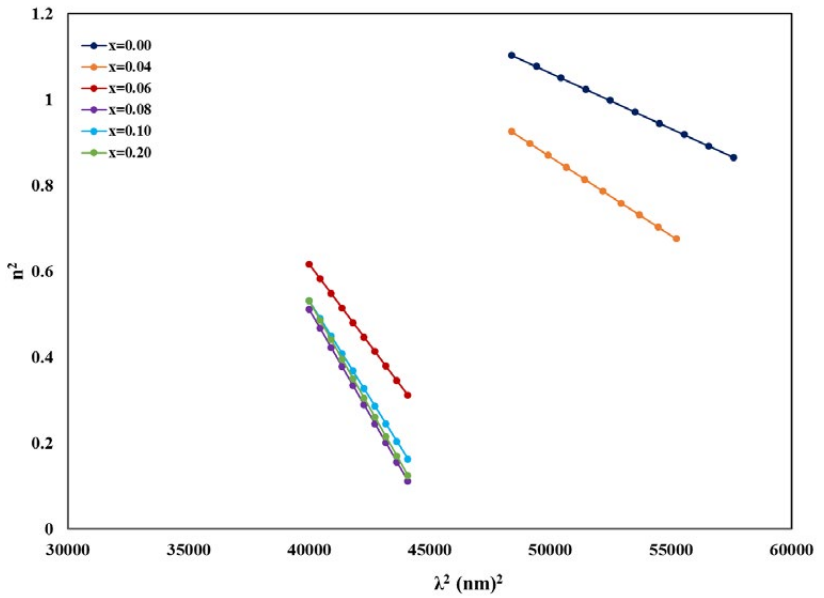

Fig. 12. Plots of n^2 as a function of l^2 for $BaZr_{1-x}Co_xO_3$ nanoparticles.

as the grain size increases. It is known that Co^{2+} ions occupy octahedral sites due to its larger ionic radius. The increase in the values of dielectric constant with the increase in the Co^{2+} content is attributed to the increase in the concentration of cobalt ions at B-sites which play a dominant role in dielectric polarization.

The magnetic properties of $BaZrO_3$ nanoparticles are dependent upon their particle sizes as well as the preparation technique. Fig. 13 illustrates the magnetic hysteresis loop for $BaZr_{1-x}Co_xO_3$ nanoparticles. It is observed the undoped sample exhibits superparamagnetism nature at room temperature. This unexpected superparamagnetic behavior may be attributed to the higher sintering temperature and the different preparation technique of the prepared sample compared with those in previous studies [30] resulting in oxygen vacancy or the interstitial position of zirconium atoms on the structure [44,45]. On the other hand, for higher Co^{2+} content (x=0.10 and 0.20) the material exhibits ferromagnetic hysteresis at room temperature. Consequently, we can conclude that $BaZrO_3$ nanoparticles substituted

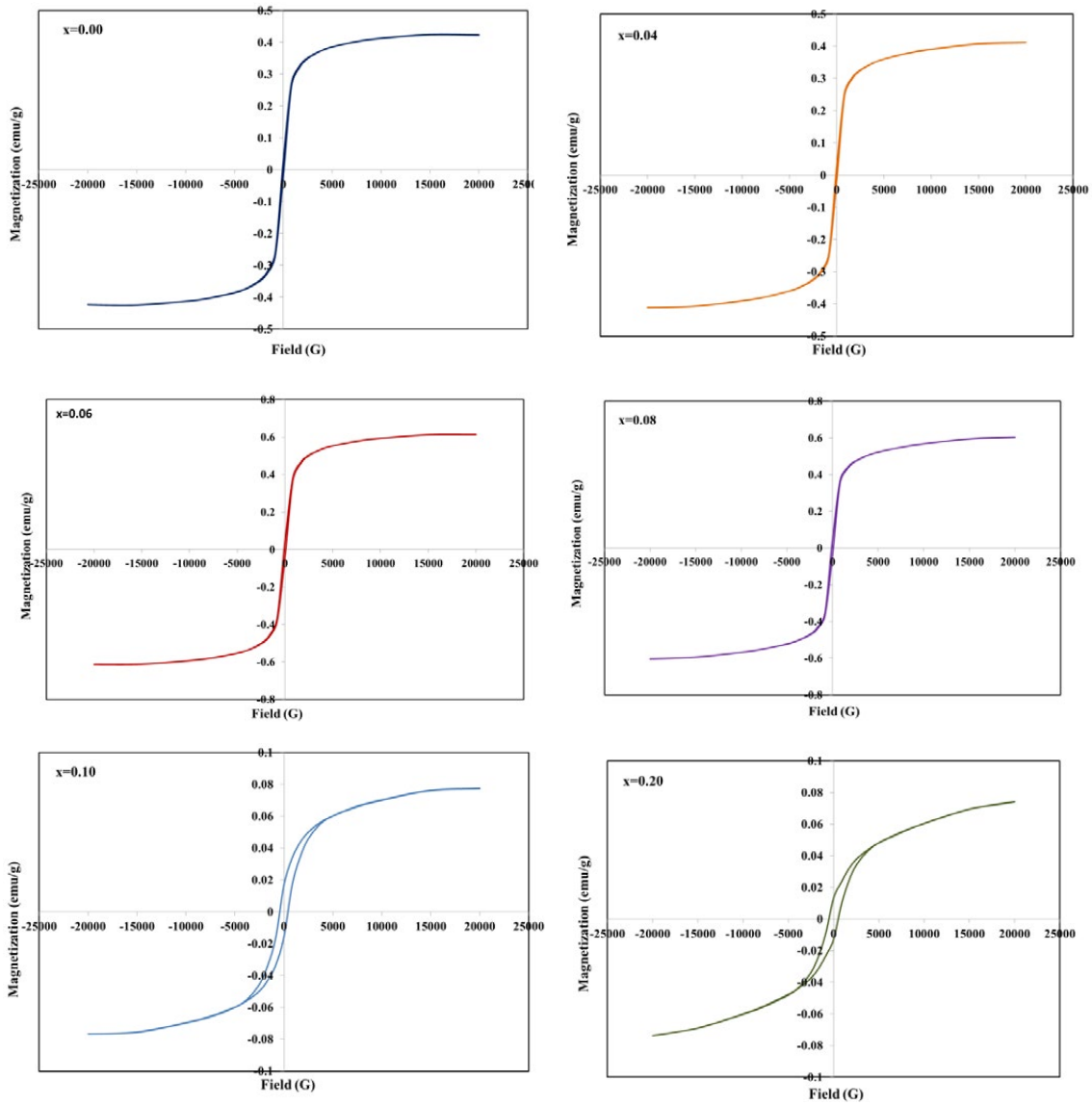

Fig. 13. Room temperature magnetic hysteresis loops (*M-H*) of $BaZr_{1-x}Co_xO_3$ nanoparticles, $0.00 \leq x \leq 0.20$.

Table 3. Values of saturation magnetization (M_s), remnant magnetization (M_r) and coercivity (H_c) of $BaZr_{1-x}Co_xO_3$ nanoparticles ($0.00 \leq x \leq 0.20$)

Co^{2+} content (x)	unit cell parameter (*a*) (A°)	t_f	D_{XRD} (nm)	$\varepsilon \times 10^{3-}$
0.00	4.185	1.091	46.218	1.14
0.04	4.183	1.100	49.519	1.28
0.06	4.182	1.105	51.353	1.12
0.08	4.181	1.109	53.328	1.18
0.10	4.179	1.115	59.001	1.32
0.20	4.171	1.139	66.982	1.35

by high Co^{2+} content are suitable for spintronic device applications. The magnetization of the samples can be explained by Neels Model [46] in which the metal ion distribution and antiparallel spin alignment of the two sublattice sites are considered. According to Neel's model, there are three types of interactions AA, AB, and BB. In fact, the intersublattice AB superexchange interaction is the most influential among them. The values of saturation magnetization (M_s), remanent magnetization (M_r) and coercivity (H_c) are evaluated and listed in Table 3. The Saturation magnetization (M_s) and remnant magnetization (M_r) values gradually increase with the increase in the Co^{2+} content till x=0.08 and then decrease with further increase in x. The increase in M_s and M_r values are attributed to the increasing A-B interaction resulting from replacement of non magnetic Zr^{4+} ions by magnetic Co^{2+} ions. On the other hand, the decrease in M_s and M_r values for high Co^{2+} content (x=0.10 and 0.20) may be due to cobalt clustering [47] which acts as a magnetically dead thin layer on the particle surface. Moreover, the other important observation is that there is an increase in coercivity as the Co^{2+} content increases. This increase in the coercivity may be attributed to the increase in the concentration of oxygen vacancies and the particle size. As a result, the coercivity of the single-domain particle assembly increases progressively as the magnetic moment of the individual particle increases, and the magnetic anisotropy energy increases.

CONCLUSIONS

In the present study, the structural, optical, and magnetic properties of the $BaZr_{1-x}Co_xO_3$ nanoparticles are investigated. The unit cell parameter, unit cell volume, average crystallite size, micro strain, and tolerance factor values change when Co^{2+} ions are doped in $BaZrO_3$ lattice, resulting in structural variation. The unit cell parameter (*a*) is observed to be decreasing linearly with Co^{2+} content obeying the Vegard's law. TEM results support the approximate sizes of the nanoparticles initially derived from XRD data. In addition, FTIR spectra show strong absorption band at 531 cm^{-1} characterizing the cubic perovskite structure of the prepared samples. From UV-vis spectra, the optical constants such as optical band gap, Urbach energy, refractive index *n* and absorption coefficient α are calculated. The Value of optical band gap is found to decrease with Co^{2+} content. On the other hand, Urbach energy are found to increase with Co^{2+} content which assures that crystal disorder increases due to defects or impurity. The data of *n* is analyzed on the basis of the single oscillator model and the values of oscillator energy E_o, dispersion energy E_d, optical energy gap E_g and lattice dielectric constant ε_l are determined. Furthermore, the magnetic measurement reveals the unexpected superparamagnetic behavior of undoped $BaZrO_3$ nanoparticles and ferromagnetic hysteresis at room temperature for $BaZr_{1-x}Co_xO_3$, x=0.10 and 0.20. The saturation magnetization increases with increasing Co^{2+} content up to 0.08 . This increase is ascribed to the increasing in the concentration of magnetic ions which enhance the inter-site exchange interaction. Thus, the value of saturation magnetization increases. Moreover, the coercivity increases with increasing Co^{2+} content due to the increase in the particle size.

ACKNOWLEDGMENT

Laboratory support and lab facilities from Central Laboratory for Water and Environmental Technology Damanhour University Faculty of Science (CLWET), which has been accredited by EGAC in compliance with the requirements of ISO/IEC 17025;2005, is gratefully acknowledged.

CONFLICT OF INTEREST

The authors declare that there are no conflicts of interest regarding the publication of this manuscript.

REFERENCES

1. Van de Krol R, Tuller HL, Electroceramics-the role of interfaces, Solid State Ion., 2002 ; 150: 167-169.
2. Kitamura M, Kobayashi M, Sakai E, Takahashi R, Lippmaa M, Determination of band diagram for a p-n junction between Mott insulator $LaMnO_3$ and band insulator Nb:$SrTiO_3$, Appl. Phys. Lett., 2015; 106 : 061605(1-5).
3. Liang YC, Integration of high-k perovskite capacitor on transparent conductive Zr-doped In_2O_3 epitaxial thin films, Thin Solid Fil., 2010; 518 : S22- S25.
4. Rubel MHK, Miura A, Takei T, Kumada N, Ali M, Nagao M, Watauchi S, Tanaka I, Oka K, Azuma M, Magome E, Moriyoshi C, Kuroiwa Y, Islam AK, Superconducting Double Perovskite Bismuth Oxide Prepared by a Low-Temperature Hydrothermal Reaction, Angew. Chem., 2014 ; 126: 3673 –3677.
5. Yamazaki Y, Hernandez-Sanche R , Haile SM, High Total Proton Conductivity in Large-Grained Yttrium-Doped Barium Zirconate, Chem. Mater.,2009; 21: 2755–2762.
6. Guo YM, Lin Y, Ran R, Shao ZP, Zirconium doping effect on the performance of proton-conducting $BaZr_yCe_{0.8-y}Y_{0.2}O_{3-\delta}$ ($0.0 \le y \le 0.8$) for fuel cell applications, J. Power Sourc., 2009 ;193 : 400-407.
7. Zhang JL, Evetts JE, $BaZrO_3$ and $BaHfO_3$: preparation, properties and compatibility with $YBa_2Cu_3O_{7-x}$, J. Mater. Sci., 1994; 29 : 778-785.
8. Erb A, Walker E, Flukiger R, The use of $BaZrO_3$ crucibles in crystal growth of the high-T_c superconductors Progress in crystal growth as well as in sample quality, Physica C, 1996 ;258 : 9-20.
9. Iwahara H, Yajima T, Hibino T, Ozaki K, Suzuki H, Protonic conduction in calcium, strontium and barium zirconates, Solid State Ion., 1993; 61: 65-69.
10. Anselmi-Tamburini U, Buscaglia MT, Viviani M, Bassoli M, Bottino C, Buscaglia V, Nanni P, Munir ZA, Solid-state synthesis and spark plasma sintering of submicron $BaY_xZr_{1-x}O_{3-x/2}$ (x = 0, 0.08 and 0.16) ceramics, J. Eur. Ceram. Soc., 2006; 26 : 2313-2318.
11. Maiti T, Guo R, Bhalla AS, Enhanced electric field tunable dielectric properties of $BaZr_xTi_{1-x}O_3$ relaxor ferroelectrics, Appl. Phys. Lett.,2007; 90 :182901(1-3).
12. Zhang Q, Zhai J, Kong LB, Relaxor Ferroelectric Materials for MicrowaveTunable applications, J. Adv. Dielectr.,2012; 2 :1230002 (1-15).
13. Viviani M, Buscaglia MT, Buscaglia V, Leoni M, Nanni P, Barium perovskites as humidity sensing materials, J. Eur. Ceram. Soc.,2001; 21 : 1981-1984.
14. Luo LB, Zhao YG, Tian HF, Yang JJ, Zhang HY, Li JQ, Ding JJ, He B, Wei SQ, Gao C, Room-temperature ferromagnetism in the Co-doped $Ba_{0.5}Sr_{0.5}TiO_3$ thin films , Appl.Phys.Lett., 2008; 92 : 232507(1-3).
15. Song C, Zeng F, Shen YX, Geng KW, Xie YN, Wu ZY, Pan F, Local Co structure and ferromagnetism in ion-implanted Co-doped $LiNbO_3$, Phys. Rev. B, 2006; 73 : 172412(1-4).
16. Lu Z, Tang Y, Chen L, Li Y, Shape-controlled synthesis and characterization of $BaZrO_3$ microcrystals, J. Cryst. Growth, 2004; 266 : 539-544.
17. Boschini F, Rulmont A, Cloots R, Vertruyen B, Rapid synthesis of submicron crystalline barium zirconate $BaZrO_3$ by precipitation in aqueous basic solution below 100 °C, J. Eur. Ceram. Soc., 2009; 29 : 1457-1462.
18. Gupta SK, Pathak N, M.Kadam R, An efficient gel-combustion synthesis of visible light emitting barium zirconate perovskite nano ceramics: Probing the photoluminescence of Sm^{3+} and Eu^{3+} doped $BaZrO_3$, J. Lumin., 2016;169 :106–114.
19. Azad AM, Subramaniam S, Synthesis of $BaZrO_3$ by a solid-state reaction technique using nitrate precursors, Mater. Res. Bull. 2002; 37 : 85-97
20. Chang I, Paek JY, Cha SW, Parametric study of Y-doped $BaZrO_3$ thin film deposited via pulsed laser deposition, J. Vac, Sci. Technol. A, 2015; 33 : 021515(1-5).
21. Sakai T, Matsumoto H, Sato Y, Hyodo J, Ito N, Hashimoto SI, Ishihara T, High Sinter ability of Planetary-Bead-Milled Barium Zirconate, Electrochemistry,2009; 77 : 876-878.
22. Bucko M, Miroslaw O, Preparation of $BaZrO_3$ nanopowders by spray pyrolysis method, J. Jan, Eur. Ceram. Soc.,2007; 27 : 3625-3628.
23. Ahmad T, Ubaidullah M , Shahazad M, Kumar D, Al-Hartomy OA, Reverse micellar synthesis, structural characterization and dielectric properties of Sr-doped $BaZrO_3$ nanoparticles, Mate. Chem. Phys.,2016;185 : 31-38.
24. Ahmad T, Ubaidullah M, Lone IH, Kumar D, Al-Hartomy OA, Microemulsion synthesis, structural characterization and dielectric properties of $Ba_{1-x}Pb_xZrO_3$ ($0.05 \le x \le 0.2$) nanoparticles, Mate. Res. Bull., 2017;89 : 185–192
25. Charoonsuk T, Vittayakorn N, Soft-Mechanochemical Synthesis of Monodispersed $BaZrO_3$ Sub-microspheres: Phase Formation and Growth Mechanism
, Mater. & Des., 2017; 118 : 44-52
26. Denton AR, Ashcroft NW, Vegard's law, Phys. Rev. A,1991; 43 : 3161-3164.
27. Parida S, Satapathy A, Sinha E, Bisen A, Rout SK, Metall. Mater. TransA,2015 ;64A : 1277-1286.
28. Zak K, Abd. Majid WH, Abrishami ME, Yousefi R, X-ray analysis of ZnO nanoparticles by Williamson–Hall and size–strain plot methods, Solid State Scie.,2011; 13 : 251-256.
29. Kumar HP, Vijayakumar C, George CN, Solomon S, Jose R, Thomasa JK, Koshy J, Characterization and sintering of $BaZrO_3$ nanoparticles synthesized through a single-step combustion process, J. Allos. Comps.,2008; 458 : 528–531.
30. Khirade PP, Birajdar SD, Shinde AB, Jadhav KM, Room temperature ferromagnetism and photoluminescence of multifunctional Fe doped $BaZrO_3$ nanoceramics, J. Alloys. Compds., 2017; 691: 287-298.
31. Chen Z, Shi E, Li W, Zheng Y, Zhong W, Hydrothermal synthesis and optical property of nano-sized $CoAl_2O_4$ pigment, Mater. Lett.,2002; 55 : 281-284.
32. Suguna S, Shankar S, Jaganathan SK, Manikandan A, Novel Synthesis and Characterization Studies of Spinel $Ni_xCo_{1-x}Al_2O_4$,(x = 0.0 to 1.0) Nano-Catalysts for the Catalytic Oxidation of Benzyl Alcohol, J. Nanoscie. Nanotec.,2018;18: 1019–1026.
33. Lee S, Woodford WH, Randall CA, Crystal and defect chemistry influences on band gap trends in alkaline earth perovskites ,App. Phys. Lett.,2008; 92 : 201909 (1-3).
34. Cavalcantea LS, Sczancoski JC, Espinosa JWM, Mastelaro VR, Michalowicz A, Pizani PS, De Vicente FS, Li MS, Varela JA, Longo E, Intense blue and green photoluminescence emissions at room temperature in barium zirconate powders, J. Alloys. Compds.,2009; 471 : 253-258.
35. Kurre R, Bajpai S, Bajpai PK, Synthesis, Characterization, Optical and

Transport Properties of $BaSnO_3$ Synthesized by Wet Chemical Route, Mater. Scie. Appl., 2018; 9: 92-110

36. Manikandan A, Vijaya JJ, Kennedy LJ, Bououdina M, Structural, optical and magnetic properties of $Zn_{1-x}Cu_xFe_2O_4$ nanoparticles prepared by microwave combustion method, J. Mol. Struct., 2013;1035 : 332–340.
37. Lin KF, Cheng HM, Hsu HC, Lin LJ, Hsieh WF, Band gap variation of size-controlled ZnO quantum dots synthesized by sol–gel method, J. Chem. Phys. Lett.,2005; 409 : 208-211.
38. Dutta K, De SK, Optical and electrical characterization of polyaniline–silicon dioxide nanocomposite, Phys. Lett. A, 2007; 361 : 141-145.
39. Zeyada HM, Makhlouf MM , Role of annealing temperatures on structure polymorphism, linear and nonlinear optical properties of nanostructure lead dioxide thin films, Opt. Mater., 2016; 54 : 181–189
40. Wemple SH, DiDomenico M, Optical Dispersion and the Structure of Solids, Phys. Rev. Lett.,1969; 23 : 1156-1160.
41. Tanaka K, Optical properties and photo induced changes in amorphous As-S films, Thin Solid Film, 1980; 66 : 271-279.
42. DiDomenico M, Wemple SH, Oxygen-Octahedra Ferroelectrics. I. Theory of Electro-optical and Nonlinear optical Effects , J. Appl. Phys.,1969; 40 : 720-734.
43. Larbi A, Khedmi N, Kanzari , The Effect of the Growth Condition on the Properties of the New Material $Sn_3Sb_2S_6$ Thin Films, Int. J. Thin Fil. Sci. Tec.,2014; 3: 27-34 .
44. Gao KH, Li ZQ, Liu XJ, Song W, Liu H, Jiang EY, Bulk $Sn_{1-x}Mn_xO_2$ magnetic semiconductors without room-temperature ferromagnetism, Solid State Commun.,2006; 138 : 175-178.
45. Srour A , Awad R , Malaeb W , Barakat MME, Physical properties of $(BaSnO_3)_x/Cu_{0.5}Tl_{0.5}Ba_2Ca_2Cu_3O_{10-d}$ super-conductor composite, J. Low Temp. Phys.,2017 ; 189 : 217 -229.
46. Neel L, Magnetic properties of ferrites: ferrimagnetism and antiferromagnetism, Ann. Phys.,1948; 3 : 137-154.
47. Poudyal and Narayan, Fabrication of superparamagnetic and Ferromagnetic Nanoparticles, (2008) pp. 16-17.